Celeroton AG
Technoparkstrasse 1
8005 Zurich
Switzerland

Transportation Electrification Conference and Expo (ITEC), 2012 IEEE

Design and Control of an Ultra High Speed Turbo Compressor for the Air Management of Fuel Cell Systems

Dongdong Zhao University of Technology of Belfort-Montbéliard, France
Daniel Krähenbühl Celeroton Ltd, Switzerland
Benjamin Blunier University of Technology of Belfort-Montbéliard, France
Christof Zwyssig Celeroton Ltd, Switzerland
Manfeng Dou Northwestern Polytechnical University, China
Abdellatif Miraoui University of Technology of Belfort-Montbéliard, France

Design and Control of an Ultra High Speed Turbo Compressor for the Air Management of Fuel Cell Systems

Dongdong Zhao,
University of Technology
of Belfort-Montbéliard,France
dongdong.zhao@utbm.fr

Krähenbühl Daniel,
Celeroton Ltd, Switzerland
daniel.kraehenbuehl@celeroton.com

Benjamin Blunier,
University of Technology
of Belfort-Montbéliard,France
Benjamin.blunier@utbm.fr

Christof Zwyssig,
Celeroton Ltd, Switzerland
christof.zwyssig@celeroton.com

Manfeng Dou,
Northwestern Polytechnical University, China
doumf@nwpu.edu.cn

Abdellatif Miraoui
University of Technology
of Belfort-Montbéliard,France
abdellatif.miraoui@utbm.fr

***Abstract*—Compressor is a crucial component of the Air Management System (AMS) used in fuel cell systems. The adoption of a turbo compressor can dramatically reduce the size of the AMS, which is a basic requirement for transportation applications. In this paper, the ultra high speed technology is employed in the compressor design, which results in ultracompact size and high efficiency. One of the main disadvantages of the turbo compressor application is the difficulty of pressure control due to the strong coupling between mass flow and pressure. A decoupling control strategy is developed so as to control the mass flow and pressure properly. The simulation results show that the mass flow and pressure can be controlled separately using two PI controllers after preliminary.**

I. Introduction

Thanks to their low temperature working condition, the proton exchange membrane fuel cells (PEMFCs) allow the system start up faster than those technologies using high temperature fuel cells, which makes it most suitable for automotive applications [1]. The air management system (Fig. 1) is one of the key equipments in the operation of a fuel cell system [2], which is used to supply oxygen to the cathode. A great deal of facilities are needed to fulfill the task of air management, among which the air compressor is a crucial component. The technical challenges and objectives for fuel cell systems in transportation applications are given by the Department of Energy (DOE) and are reported in [1]. Automotive fuel cell industry needs a compact, lightweight, low-cost and high efficiency compressor. This can be achieved by using turbo compressor instead of scroll, lobe, or screw compressor, increasing the rotational speed [3]. A scroll compressor is employed in [1], [4], [5]. In [6], a twin-screw compressor is used for the high-pressure condition and a blower is used for the low-pressure condition. Screw or roots-type superchargers are commonly chosen for their easier technical implementation. The turbo compressor has major advantages of compactness and efficiency over other compressor types, whereas it is more critical to implement in terms of pressure and surge control because of the strong coupling between mass flow and pressure.

This paper focus on the design and control of an ultra high speed turbo compressor used in air management system. The main objective of the compressor design is to reduce the size and weight so as to make it feasible for transportation application, which is achieved by increasing the rotational speed. The objective of the compressor control is to provide proper mass flow and pressure which fuel cell needs according to the load demands. In this paper, a dynamic decoupling controller based on neural network is proposed to deal with the problem of strong coupling so as to control the mass flow and pressure separately.

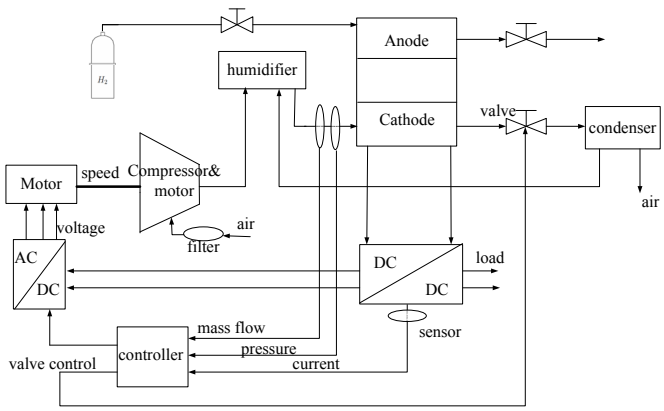

Fig. 1. Air management system

II. Compressor Design

A. Scaling of turbo compressor and electric motor

Turbo compressors for fuel cell applications demand low mass flow rates (10 to 30 g/s) at relatively high pressure ratios (1 to 2). For a standard speed turbo compressor (e.g. 3,000

to 30,000 rpm) these specifications result in a very low flow coefficient:

$$\phi_{t1} = \frac{\dot{V}_{t1}}{d_2^2 u_2} = \frac{\dot{m}}{\rho_{t1} d_2^2 u_2} = \frac{\dot{m}\omega^2}{\rho_{t1} 4 u_2^3} \tag{1}$$

where $\dot{V}_{t1}$ is the total inlet volume flow in (m^3/s), ρ_{t1} is the total inlet density in (kg/m^3), $\dot{m}$ is the mass flow rate in (kg/s), u_2 is the impeller circumferential speed at the impeller radius $d_2/2$ and ω the rotational speed. This low flow coefficient then results in a very low efficiency according to [7]. The ideal flow coefficient for radial turbo compressor and with this a higher efficiency, is reached by increasing the rotational speed. A further advantage of this high rotational speed is the decrease of the impeller radius and therefore an increase in power density in turbo machinery. Also the electrical motor power density is roughly proportional to the speed.

$$\frac{P}{V} \propto n \tag{2}$$

Therefore, the overall volume and weight of a high-speed electrically drive turbo compressor is several times lower than of a scroll or displacement compressors with the same specifications for pressure ratio and mass flow which are not capable of running at high speed [3]. A further advantage is the low noise of a high-speed turbo compressor, compared to standard scroll or displacement compressors, because the vibrations are both smaller and can be damped more efficiently due to the high frequency.

B. Turbo compressor design

The compressor is designed for fuel cell applications, and is therefore designed for a rated mass flow of 12 g/s and a rated pressure ratio of 1.5. The inlet conditions are ambient pressure (1 bar) and 25 °C. The turbo compressor system consists of a radial impeller with splitter blades but no shroud, a vaneless diffuser and a spiral casing. Retaining an ideal flow coefficient of 0.085, results in a turbo compressor with an impeller diameter of 21 mm and a rotational speed of 250,000 rpm. The assumed isentropic total-total efficiency is 74 % [7] while the rated compressor power is 580 W. The impeller optimization has been carried out with a 2D-throughflow code [8] and verified with 3-D computational fluid dynamics (CFD) simulations. The compressor and power map data for different rotational speeds and variable mass flow is calculated with a 1D-analytical design tool including correction factors based on empirical data from similar small high-speed compressors [9]. The compressor map gets computed only from the design point. In Fig. 5(a) the comparison between the 1D-analytical compressor map and the measured compressor map is shown.

C. Electrical machine design

The electrical machine is designed for the rated specifications defined by the turbo compressor design: a rotational speed of 250,000 r/min and a shaft power of 580 W. The electrical machine design comprises several challenges such as the mechanical rotor design, particularly the stresses in the PM and the retaining titanium sleeve, additionally, high rotational speeds usually increases the losses, mainly due to eddy current effects in winding, stator iron and the entire rotor (magnet, iron, sleeves), but also in higher air friction losses. Increasing the speed with constant efficiency also results in higher loss density, or higher losses per surface area, therefore a thermal design is required. For this reason, an optimization method has been developed, which takes air-friction losses, iron losses, copper losses, and eddy-current losses into account [10]. The rotor losses due to armature reaction is not part of the optimization process, but is calculated after optimization process. The stator magnetic field rotates with a high frequency (4.2 kHz); it is therefore necessary to minimize the losses in the stator core by using amorphous iron and the eddy-current losses in the skewed air-gap winding by using litz wire.

The rotor of the PM motor consists of a diametrically magnetized, not segmented cylindrical, SmCo PM encased in a retaining titanium sleeve ensuring sufficiently low mechanical stresses on the magnet (see Fig. 2). The eccentricity is minimized by shrink-fitting the sleeve onto the PM and grinding the rotor. The two high-speed ball bearings are assembled at each end of the rotor in order to be able to change them without the need for disassembling the impeller. Besides the

Fig. 2. Assembled rotor including impeller and high-speed ball bearings

design of the individual components, rotor dynamics of the common rotor of the electrical machine and the turbo machine is required. The critical speeds of the rotor are depicted in Fig. 3. The critical speeds modes' calculations have been made during the electrical machine optimization process with an analytical approach in order to define geometric constraints for the machine. The final rotor dynamic design has been verified with 3-D finite-element (FE) simulations. The rotor is designed such that the nominal speed of 250,000 r/min is below the first bending mode (third critical speed), but above the two first critical speeds.

D. Realization and measurements

The realized compressor prototype (Fig. 4) has a weight of 0.6 kg which is fifty times lower than a comparable scroll compressor. The compressor has been evaluated on a test bench. The measurement of the compressor and power map data is in very good agreement with the calculations as can be seen in Fig. 5. The measured compressor efficiency in the

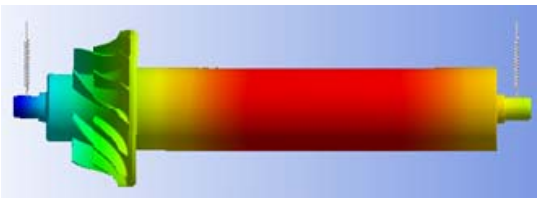

(a) First critical speed at 1.1 kHz, 66 000 r/min

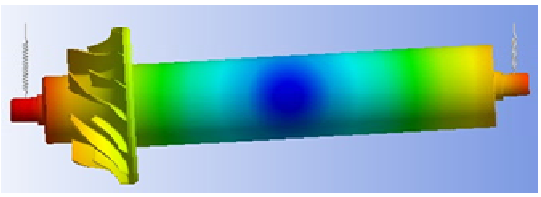

(b) second critical speed at 2.6 kHz, 156 000 r/min

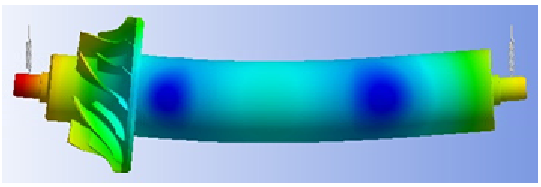

(c) third critical speed at 8 kHz, 480 000 r/min

Fig. 3. Critical speeds of the turbo compressor rotor. (Blue) No displacement. (Red) Maximal displacement

rated operating point (250,000 rpm, 11.4 g/s, pressure ratio of 1.5, inlet temperature 300 K) is 74.8 % which is also very close to the designed efficiency. The motor and converter efficiency in the rated operating point is 92 % and 90.6 % respectively. This results in a total system efficiency of 62.3 %.

Fig. 4. Compressor prototype

III. System Modeling and Controller Design

A. Model of the manifold

The manifold represents the lumped volume of the pipes between the compressor and the fuel cell stack. The dynamics of the air pressure in the manifold directly relate to compressor characteristics. According to the mass conservation principle, the dynamics of the air mass m accumulated in the manifold volume and the manifold pressure p can be expressed through

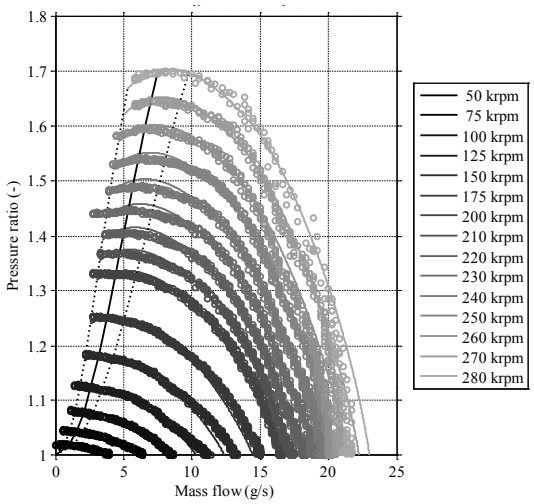

(a) Calculated and measured compressor map

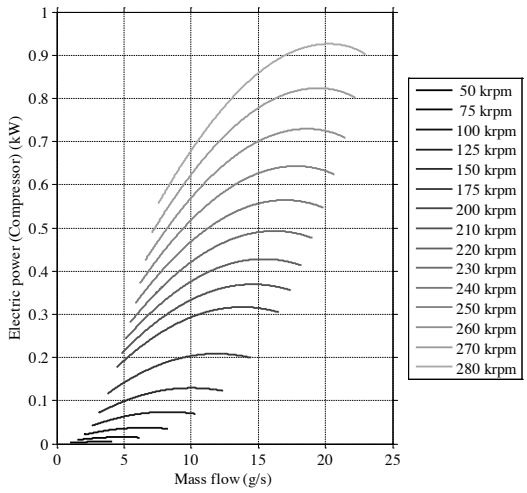

(b) Calculated power map of the compressor

Fig. 5. Compressor maps

the following equations [11], [12], [13]:

$$\frac{\mathrm{d}m}{\mathrm{d}t} = q - q_{out} \tag{3}$$

$$\frac{\mathrm{d}p}{\mathrm{d}t} = \frac{\gamma R_a}{V}(qT_{in} - q_{out}T_{out}) \tag{4}$$

where q and q_{out} are the air mass flow into and out of the manifold respectively. T_{in}, T_{out} are the compressor outlet gas temperature and manifold air temperature respectively. γ is the thermal ratio coefficient of the air and R_a is the gas constant of the air. V is the manifold volume. In the case of air, $\gamma = 1.4, R_a = 8.3$. In this paper, the air temperature in the manifold is assumed to be constant and equal to the compressor outlet air temperature. That is $T_{in} = T_{out} = T$. Then, (4) can be expressed as follows:

$$\frac{\mathrm{d}p}{\mathrm{d}t} = \frac{R_a T}{V}(q - q_{out}) \tag{5}$$

The nozzle flow equation is used to calculate q_{out}, which

is divided into two regions by the critical pressure ratio ξ.

$$\xi = \left(\frac{p_{atm}}{p}\right)_{crit} = \left(\frac{2}{\gamma+1}\right)^{\frac{\gamma}{\gamma-1}} \tag{6}$$

For $\frac{p_{atm}}{p} > \xi$,

$$q_{out} = p \cdot S_{ctrl}(\theta)\sqrt{\frac{2\gamma M_{air}}{(\gamma-1)RT}\left[\left(\frac{p_{atm}}{p}\right)^{\frac{2}{\gamma}} - \left(\frac{p_{atm}}{p}\right)^{\frac{\gamma+1}{\gamma}}\right]} \tag{7}$$

For $\frac{p_{atm}}{p} \leq \xi$,

$$q_{out} = p \cdot S_{ctrl}(\theta)\sqrt{\frac{2\gamma M_{air}}{(\gamma-1)RT}} \tag{8}$$

where θ, p_{atm}, $M_{air} = 29\,\text{g/mol}$ are the open angle of valve, atmosphere pressure and molar mass of air respectively. Then, the critical pressure ratio ξ is calculated equal to 0.528. $S_{ctrl}(\theta)$ is the open area of the valve:

$$S_{ctrl}(\theta) = \pi \cdot r \cdot \theta \tag{9}$$

where r is the radius of the valve. In this paper, the pressure p is below 1.8. Assuming $p_{atm} = 1$, gives $\frac{p_{atm}}{p} > 1/1.8 > 0.528$. Therefore, only (7) is used in the mathematical model. According to the analysis above, the lumped formulation of q_{out} can be expressed as follows:

$$q_{out} = \varphi(\theta, p) \tag{10}$$

B. System analysis

The control target is to make the mass flow q and pressure ratio p track the references, which change according to the load situation. The control variables are the compressor speed ω_{cp} and the valve open angle θ. At an operating point, the linearized formulation of the system can be expressed as follows:

$$\begin{bmatrix} q \\ p \end{bmatrix} = \begin{bmatrix} G_{p11}(s) & G_{p12}(s) \\ G_{p21}(s) & G_{p22}(s) \end{bmatrix} \begin{bmatrix} \omega_{cp} \\ \theta \end{bmatrix} \tag{11}$$

Here we define

$$G_p(s) = \begin{bmatrix} G_{p11}(s) & G_{p12}(s) \\ G_{p21}(s) & G_{p22}(s) \end{bmatrix} \tag{12}$$

Using relative gain array RGA method in control theory [14], the interaction among multiple control loops is quantitatively analyzed. The RGA is a 2×2 matrix for a two inputs two outputs system.

$$RGA = \begin{bmatrix} \lambda_{11} & \lambda_{12} \\ \lambda_{21} & \lambda_{22} \end{bmatrix} \tag{13}$$

where

$$\lambda_{ij} = \frac{\frac{\partial y_i}{\partial u_j}|_{u_r=cont}, (r \neq j)}{\frac{\partial y_i}{\partial u_j}|_{y_r=cont}, (r \neq i)}, i = 1, 2; j = 1, 2$$

where y_1, y_2 represent the system outputs q and p respectively. u_1, u_2 represent the control inputs ω and θ respectively. However, this system is highly nonlinear which means that the matrix $G_p(s)$ is not constant. $G_p(s)$ changes as the operating points change. In order to analyze system nonlinear characteristic, the Simulink LTI toolbox is used to linearize the system at different operating points. Part of RGA is listed in TABLE I which shows that at different operating points the degree of coupling is different. At a specific pressure ratio, the lower mass flow the stronger coupling exist. Therefore, a static decoupling control is not feasible.

TABLE I
DYNAMIC RGA TABLE

p=1.40			p=1.30		
q (g/s)	RGA		q (g/s)	RGA	
15.85	0.6959	0.3041	15.89	0.7279	0.2721
	0.3041	0.6959		0.2721	0.7279
14.86	0.6679	0.3321	14.96	0.7008	0.2992
	0.3321	0.6679		0.2992	0.7008
13.87	0.6361	0.3639	13.89	0.6716	0.3284
	0.3639	0.6361		0.3284	0.6761
12.88	0.6023	0.3639	12.08	0.6030	0.3907
	0.3639	0.6023		0.3907	0.6030
9.88	0.5655	0.4345	9.98	0.5641	0.4359
	0.4345	0.5655		0.4359	0.5641

C. Controller design

The control system (Fig. 6) consists of three parts: dynamic decoupling, motor controller and valve controller. Vector control is employed in the motor controller to drive the compressor and PI control is adopted for the valve position regulation. The motor controller and valve controller are well designed, so that both the compressor speed and the valve position have good reference tracking characteristics. This paper focus on the development of the dynamic decoupling, which is employed to deal with the strong coupling problem between mass flow and pressure so as to control them separately.

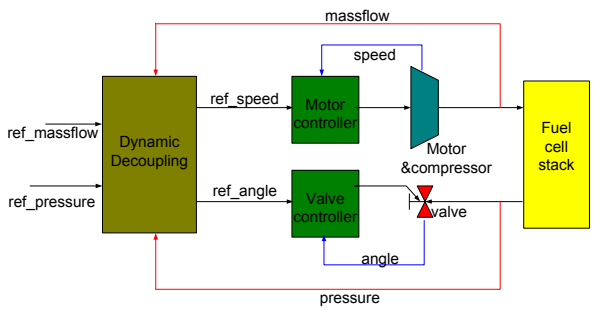

Fig. 6. Air management system controller

According to the system analysis, traditional static decoupling is not feasible because of the coupling degree is not a constant. On the basis of the traditional static decoupling, a dynamic decoupling based on neural network is proposed (see Fig. 7). After the implementation of the decoupling matrix $N(s)$, the compressor speed and the valve angle can be obtained as follows:

$$\begin{bmatrix} \omega_{cp} \\ \theta \end{bmatrix} = \begin{bmatrix} N_{11}(s) & N_{12}(s) \\ N_{21}(s) & N_{22}(s) \end{bmatrix} \begin{bmatrix} U_{c1} \\ U_{c2} \end{bmatrix} \tag{14}$$

TABLE II
TRANSFER GAINS AT DIFFERENT OPERATING POINTS

q (g/s) \ **p** (-)	1.5		1.3		1.2	
13.0	$4.424e-05$	1.177	$4.978e-05$	0.6890	$5.311e-05$	0.4342
	$3.620e-06$	-0.05970	$2.452e-06$	-0.03996	$1.768e-06$	-0.02689
12.0	$4.221e-05$	1.289	$4.803e-05$	0.7720	$5.160e-05$	0.4942
	$3.741e-06$	-0.05485	$2.563e-06$	-0.03887	$1.861e-06$	-0.02697
11.0	$3.994e-05$	1.408	$4.601e-05$	0.8670	$4.983e-05$	0.5653
	$3.862e-06$	-0.04822	$2.678e-06$	-0.03687	$1.960e-06$	-0.02663
10.0	$3.741e-05$	1.537	$4.368e-05$	0.9751	$4.774e-05$	0.6502
	$3.979e-06$	-0.03940	$2.797e-06$	-0.03363	$2.066e-06$	-0.02563
9.0	$3.460e-05$	1.670	$4.102e-05$	1.096	$4.528e-05$	0.7502
	$4.090e-06$	-0.02796	$2.918e-06$	-0.02872	$2.177e-06$	-0.02363
8.0	$3.151e-05$	1.805	$3.796e-05$	1.230	$4.239e-05$	0.8671
	$4.190e-06$	-0.01351	$3.038e-06$	-0.02160	$2.293e-06$	-0.02029

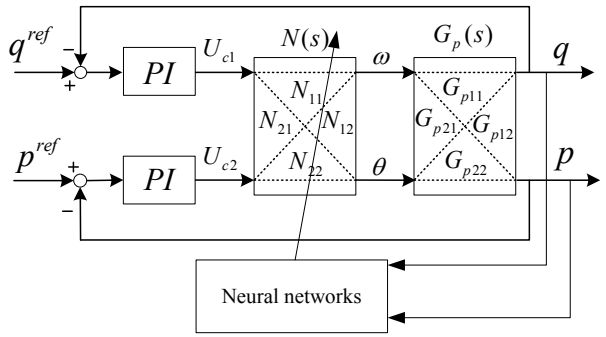

Fig. 7. Dynamic decoupling

where U_{c1} and U_{c2} are the outputs of the PI control as shown in Fig. 7. According to (11) and (14), the decoupling matrices are obtained:

$$\begin{bmatrix} N_{11}(s) & N_{12}(s) \\ N_{21}(s) & N_{22}(s) \end{bmatrix} = \begin{bmatrix} G_{p11}(s) & G_{p12}(s) \\ G_{p21}(s) & G_{p22}(s) \end{bmatrix}^{-1} \Lambda \quad (15)$$

where

$$\Lambda = \begin{bmatrix} G_{11}(s) & 0 \\ 0 & G_{22}(s) \end{bmatrix} \quad (16)$$

After decoupling, the system outputs can be expressed as follows:

$$\begin{bmatrix} q \\ p \end{bmatrix} = \begin{bmatrix} G_{11}(s) & 0 \\ 0 & G_{22}(s) \end{bmatrix} \begin{bmatrix} U_{c1} \\ U_{c2} \end{bmatrix} \quad (17)$$

Then q and p can be controlled by U_{c1} and U_{c2} respectively. In view of the dynamic characteristic of $G_p(s)$, corresponding decoupling matrices $N(s)$ are obtained by means of a neural network which is trained off line to fulfill dynamic decoupling. The structure of the neural network, which is trained using Back Propagation (BP) algorithm, is shown in Fig. 8. The inputs are the operating points (q, p), and the outputs are the decoupling matrices. In order to simplify calculations, static gains, ($P1, P2, P3, P4$), are used to replace the transfer functions, ($N_{11}(s), N_{12}(s), N_{21}(s), N_{11}(s)$). TABLE II gives part of the static transfer gains, which are obtained by linearizing the system at different operating points. It should be noticed that, this replacement may lead to the instability of the system. In this paper, $G_{11}(s), G_{11}(s)$ are designed appropriately according to the order of $G_p(s)^{-1}$ to ensure the stability of the system.

$$\begin{bmatrix} G_{11}(s) & 0 \\ 0 & G_{22}(s) \end{bmatrix} = \begin{bmatrix} \frac{1}{s+1} & 0 \\ 0 & \frac{1}{(s+1)^2} \end{bmatrix} \quad (18)$$

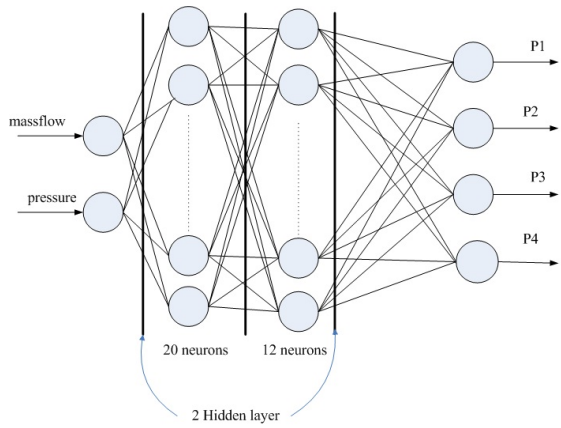

Fig. 8. Neural network model

IV. SIMULATION RESULTS

Computer simulation is performed to verify the effectiveness and behavior of the proposed control strategy. The simulation results are shown in Fig. 9. In order to test the influence of sudden change of mass flow to pressure ratio, a step change of mass flow reference is given at 10 s. The zoom of corresponding deviation of pressure is shown in Fig. 10(b). In the same way, the sudden change of pressure ratio is executed at 14 s. The corresponding deviation of mass flow is zoomed in as shown in Fig. 10(a). The results show that the pressure can be maintained constant when the mass flow varies. Furthermore, sudden change of mass flow (pressure ratio) has a very weak influence on the pressure ratio (mass flow).

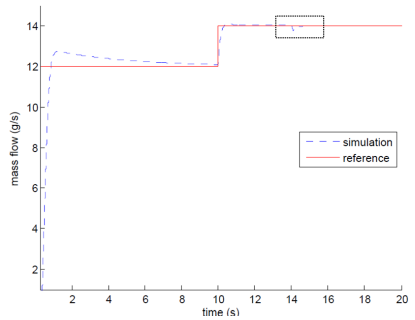

(a) Mass flow response

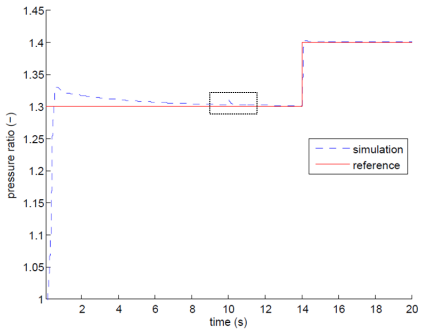

(b) Pressure ratio response

Fig. 9. Simulation of mass flow and pressure tracking characteristics

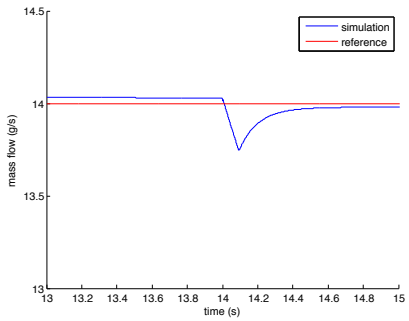

(a) Zoom of mass flow fluctuation in Fig.9(a)

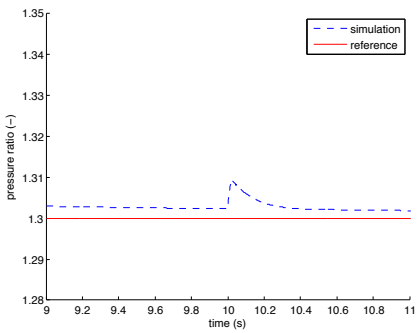

(b) Zoom of pressure ratio fluctuation in Fig.9(b)

Fig. 10. Zoom of deviations shown in Fig.9

V. Conclusion

In this paper, an ultra high speed turbo compressor is designed to fulfill the requirement of compactness for automotive applications. The challenges of ultra high speed turbo compressor design such as the mechanical rotor construction, the rotor dynamic design, the minimization of the losses in the electric motor are highlighted and corresponding solutions have been come up with. The size and weight meet the requirements of DOE. At the same time, the high efficiency dramatically reduces the parasitic power consumption of fuel cell systems. Both the strong coupling and highly nonlinear characteristics result in the difficulty of the pressure control. The coupling and nonlinear characteristics are analyzed by linearizing the system at different operating points. On the basis of linearization data, a dynamic decoupling controller based on neural network is designed. The simulation results show that after decoupling the mass flow and pressure can be controlled separately using two PI controllers.

References

[1] B. Blunier and A. Miraoui, "Proton exchange membrane fuel cell air management in automotive applications," *Journal of Fuel Cell Science and Technology*, vol. 7, no. 041007, p. 041007, 2010.

[2] A. Vahidi, A. Stefanopoulou, and H. Peng, "Model predictive control for starvation prevention in a hybrid fuel cell system," in *Proc. American Control Conf the 2004*, vol. 1, pp. 834–839.

[3] D. Krähenbühl, C. Zwyssig, H. Weser, and J. Kolar, "A miniature 500 000-r/min electrically driven turbocompressor," *Industry Applications, IEEE Transactions on*, vol. 46, no. 6, pp. 2459–2466, 2010.

[4] B. Blunier, M. Pucci, G. Cirrincione, M. Cirrincione, and A. Miraoui, "A scroll compressor with a high-performance sensorless induction motor drive for the air management of a pemfc system for automotive applications," vol. 57, no. 6, pp. 3413–3427, 2008.

[5] B. Blunier, G. Cirrincione, Y. Hervé, and A. Miraoui, "A new analytical and dynamical model of a scroll compressor with experimental validation," *International Journal of Refrigeration*, vol. 32, no. 5, pp. 874–891, 2009.

[6] J. Cunningham, M. Hoffman, and D. Friedman, "A comparison of high-pressure and low-pressure operation of pem fuel cell systems," 2001.

[7] M. Casey and C. Robinson, "A guide to turbocharger compressor characteristics," in *Dieselmotorentechnik, 10th Symposium (Ed. M. Bargende)*, 2006, pp. 30–31.

[8] ——, "A new streamline curvature throughflow method for radial turbomachinery," *Journal of Turbomachinery*, vol. 132, p. 031021, 2010.

[9] M. V. Casey and C. J. Robinson, "A method to estimate the performance map of a centrifugal compressor stage," in *Proc. of the ASME Turbo Expo 2011, Vancouver, Canada.*

[10] J. Luomi, C. Zwyssig, A. Looser, and J. Kolar, "Efficiency optimization of a 100-w 500 000-r/min permanent-magnet machine including air-friction losses," *Industry Applications, IEEE Transactions on*, vol. 45, no. 4, pp. 1368–1377, 2009.

[11] A. Vahidi, I. Kolmanovsky, and A. Stefanopoulou, "Constraint management in fuel cells: A fast reference governor approach," in *American Control Conference, 2005. Proceedings of the 2005*. IEEE, 2005, pp. 3865–3870.

[12] J. Pukrushpan, "Modeling and control of fuel cell systems and fuel processors," *Amercia: The University of Michigan*, 2003.

[13] M. Grujicic, K. Chittajallu, E. Law, and J. Pukrushpan, "Model-based control strategies in the dynamic interaction of air supply and fuel cell," *Proceedings of the Institution of Mechanical Engineers, Part A: Journal of Power and Energy*, vol. 218, no. 7, pp. 487–499, 2004.

[14] S. Skogestad and M. Morari, "Implications of large rga-elements on control performance," *Industrial & engineering chemistry research*, vol. 26, no. 11, pp. 2323–2330, 1987.